

Limited thermal and spin transport in a dissipative superfluid junction

Meng-Zi Huang^{†,*}, Philipp Fabritius^{†,‡}, Jeffrey Mohan,[§] Mohsen Talebi, Simon Wili, and Tilman Esslinger
Institute for Quantum Electronics and Quantum Center, ETH Zurich, 8093 Zurich, Switzerland
 (Dated: 2024-12-10)

Limited transport occurs in various systems when microscopic details give way to fundamental principles, ranging from quantized conductance for fermions in one dimension to quantum-limited sound and spin diffusivity in strongly interacting Fermi gases. However, limited transport in dissipative open quantum systems is rare due to the lack of many conservation laws. In particular, thermal and spin transport in interacting systems under particle dissipation are largely unexplored. Here we observe dissipation-induced but limited thermal and spin transport through a dissipative one-dimensional junction connecting two superfluids of unitary Fermi gases. The thermal and spin conductances of the superfluid junction increase sharply with particle dissipation and seemingly approach values for a non-dissipative, non-interacting system—limited due to quantum confinement of the junction. This behavior is independent of the dissipation mechanism, being either spin-dependent or pairwise losses. This work may inform theories on interacting open quantum systems and opens up perspectives for dissipative control of spin and thermoelectric transport.

Transport phenomena that exhibit robust, bounded conductances often arise from fundamental principles. For example, the fermionic nature gives rise to quantized conductance in one-dimensional systems without interactions. In strongly interacting Fermi gases, sound diffusivity [1–3], spin diffusivity [4, 5], and shear viscosity [6, 7] reach quantum-limited values, originating from hydrodynamics and the lack of quasiparticles [8, 9]. This also connects to the so-called Planckian dissipation in strongly correlated electronic systems that hints at a much deeper principle [10]. However, in open quantum systems with particle dissipation, the absence of particle and energy conservation makes the existence of limited transport more elusive [11]. Notably, the quantum Zeno effect can give rise to bounded dissipation but the limits are not robust and result from competition of timescales [12, 13]. More interestingly, thermal and spin transport can, particularly for interacting superfluid systems, reveal the defining features of the interplay between dissipation and the superfluid order [14–16]. It is an interesting open question whether limited transport can arise in these open systems.

Cold-atoms experiments offer well controlled platforms for studying interacting quantum many-body systems with dissipation. For example, dissipation can probe the microscopic properties and induce emergent dynamics in many-body systems [17–23]. Although thermal and spin transport have been studied in closed systems in near-equilibrium strongly interacting gases [2, 3, 5] as well as in far-from-equilibrium settings [4, 24–27], their studies in open systems with controlled dissipation remain challenging, especially for bulk experiments that are sensitive to excessive heating. Here, we combine local dissipation

with two-terminal measurements of particle, entropy, and spin currents. Going beyond previous studies of dissipative junctions using only particle transport in the weakly interacting [28] and strongly-interacting [29, 30] regimes, the combined measurements of thermal and spin transport reveal an unexpected state of the strongly interacting fermionic system with limited thermal and spin conductances.

We focus on the superfluid regime of the unitary Fermi gas [31], which shows distinct transport phenomena in a quasi-one-dimensional (quasi-1D) ballistic junction, including enhanced particle current [32, 33] and the suppression of spin and thermal diffusion [16, 24, 27, 34, 35]. In particular, particle transport in this superfluid junction displays a nonlinear current-bias relation, bearing similarities to the subgap transport in superconducting quantum point contacts [36, 37]. This has led to attempts of microscopic understanding based on Multiple Andreev reflections (MAR) that reproduces the nonlinear current response [33]. Yet, the MAR picture was confronted by recent measurements of nonlinear entropy current through the junction [27]. The physics of this strongly interacting, far-from-equilibrium system, arguably very different from conventional superconductors, is still an open question.

The observed entropy current [27] is *advective*—entropy is carried by the particle current—and is abnormally large for superfluid reservoirs, meaning a large Seebeck coefficient [38]. However, the thermal conductance, i.e., how fast entropy diffuses without net particle flow, is instead suppressed in the quasi-1D superfluid junction. These two modes of entropy transport, advective and diffusive, can be discriminated in the experiment given their distinct timescales in the 1D limit [27]. As a result, thermal conductance can be extracted with the help of a phenomenological model that is similar to conventional thermoelectrics [38], but modified with a nonlinear advective term to incorporate the nonlinear response [27].

In the present work, we engineer particle dissipation

[†] These authors contributed equally to this work

* mhuang@phys.ethz.ch

[‡] Present address: X-Rite Europe GmbH, Regensdorf, Switzerland

[§] Present address: Welinq SAS, Paris, France

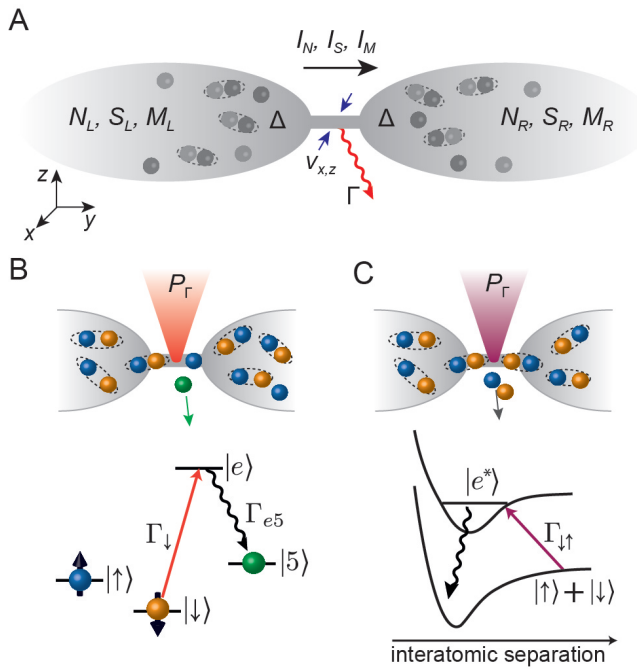


FIG. 1. **Scheme to measure transport coefficients of a superfluid junction in the presence of engineered spin-dependent or pairwise dissipation.** (A) Measuring entropy I_S , particle I_N and spin I_M currents probes the dissipative, quasi-1D channel (transversal confinement $h\nu_{x,z} \gtrsim 5k_B T$) connecting two fermionic superfluid reservoirs (L and R) with pairing gap $\hbar\Delta \gg k_B T$ near the entrance to the channel. The local particle loss rate Γ is engineered via spin-dependent (B) and pairwise (C) dissipation, realized by a focused laser beam inside the channel with a waist smaller than the channel length. (B,C) Illustration and energy diagram of the optical pumping process (B) with rate Γ_{\downarrow} used to produce spin-dependent particle losses and the photoassociation of molecules $\Gamma_{\uparrow\downarrow}$ (C) used to realize strictly pairwise losses.

inside the superfluid junction and observe a sharp increase in thermal and spin diffusive transport. The locality of the dissipation allows us to alleviate detrimental heating to the overall system which generally challenges experiments with dissipation. Dissipation switches the junction from an insulator for thermal and spin diffusion to a conductor. Interestingly, both the thermal and spin conductances approach the quantum-limited values for a non-interacting system without dissipation [39, 40] or a quantum critical liquid [41]. We compare two distinct dissipation mechanisms in regard to the superfluid order parameter—a spin-dependent loss that dissipate one spin more than the other, leaving some broken pairs; and pairwise losses that are strictly spin correlated. Interestingly, they show similar effects on spin and thermal diffusion and approach the same limit.

We start all measurements by preparing a degenerate Fermi gas of ${}^6\text{Li}$ in a balanced mixture of the lowest ($|\downarrow\rangle$) and third-lowest ($|\uparrow\rangle$) hyperfine ground states in the unitary regime (Feshbach resonance at 689 Gauss) with an

initial total atom number $N = N_{\downarrow} + N_{\uparrow} = 2.9(2) \times 10^5$. The gas is trapped in a near-harmonic trap separated into two halves along the y axis by two intersecting repulsive TEM₀₁-like beams. This forms two reservoirs, left (L) and right (R), connected by a ballistic channel. The transverse confinement of the channel is in the quasi-1D limit with trapping frequencies $\nu_z = 9.4(1)$ kHz along z and $\nu_x = 10.9(2)$ kHz along x ($h\nu_{x,z} \gtrsim 5k_B T$) [27, 33]. Transport between the reservoirs can be initiated by preparing different types of imbalances between the reservoirs [42]. An attractive “gate” beam covering the channel region is used to adjust the local chemical potential during transport. After transport between the reservoirs for a time t , we perform thermometry of each reservoir in a half harmonic trap, by adiabatically removing the channel confining beams while keeping the two reservoirs separated by a thin “wall” beam [27]. As the entropy $S_i = S_{i,\uparrow} + S_{i,\downarrow}$ and atom number $N_i = N_{i,\uparrow} + N_{i,\downarrow}$ in each reservoir ($i = L, R$) are conserved between the end of transport and imaging [42], we use these two thermodynamic quantities to describe the reservoirs throughout the paper. The prepared reservoirs typically have an initial degeneracy of $T/T_F = 0.21(1)$, corresponding to an average entropy of $s = S/Nk_B = 1.58(6)$ which is below the superfluid transition at $s_c = 1.9(1)$ in our trap [27]. For a first set of measurements, an entropy imbalance ($\Delta S = S_L - S_R > 0$) between the reservoirs is prepared while keeping the atom number imbalance minimal, $\Delta N = N_L - N_R \approx 0$. This initial state allows us to measure the advective and diffusive response of the system [27, 34]. For a second set of measurements, we prepare a pure magnetization imbalance $\Delta M = M_L - M_R \neq 0$, where $M_i = N_{i,\uparrow} - N_{i,\downarrow}$, with negligible atom number and entropy imbalances $\Delta N \approx \Delta S \approx 0$. This preparation allows us to probe the spin diffusion under the same conditions of the channel [24, 27].

To realize controlled particle dissipation inside the channel, a resonant laser beam propagating along z is tightly focused into the channel with a $1/e^2$ beam radius of $w_{\Gamma} = 1.3(1)$ μm , similar to the channel width and shorter than the channel length. Two distinct types of dissipation are achieved with this beam by tuning its frequency. Firstly, spin-dependent particle loss is engineered by a resonant excitation of $|\downarrow\rangle$, optically pumping the atoms to an auxiliary ground state that leaves the system (Fig. 1B) [29] with a single-atom photon scattering rate Γ_{\downarrow} . Due to attractive interactions, atoms of the other spin $|\uparrow\rangle$ are also lost, though at a lower rate of $0.83(4) \cdot \Gamma_{\downarrow}$. Secondly, pairwise loss is engineered via a photoassociation transition that excites a pair of $|\uparrow\rangle$ and $|\downarrow\rangle$ to an excited molecular state [17, 43, 44] which subsequently leaves the trap (Fig. 1C) with a photon-scattering rate $\Gamma_{\uparrow\downarrow}$. The loss rate $\Gamma_{\uparrow\downarrow}$ depends on both the atomic density and the pair correlations and thus on Tan’s contact [45]. While an *ab initio* calculation of the scattering rate $\Gamma_{\uparrow\downarrow}$ is beyond the scope of this paper, we rely on the measured atom loss for comparison between $\Gamma_{\uparrow\downarrow}$ and Γ_{\downarrow} . The power of the dissipative beam

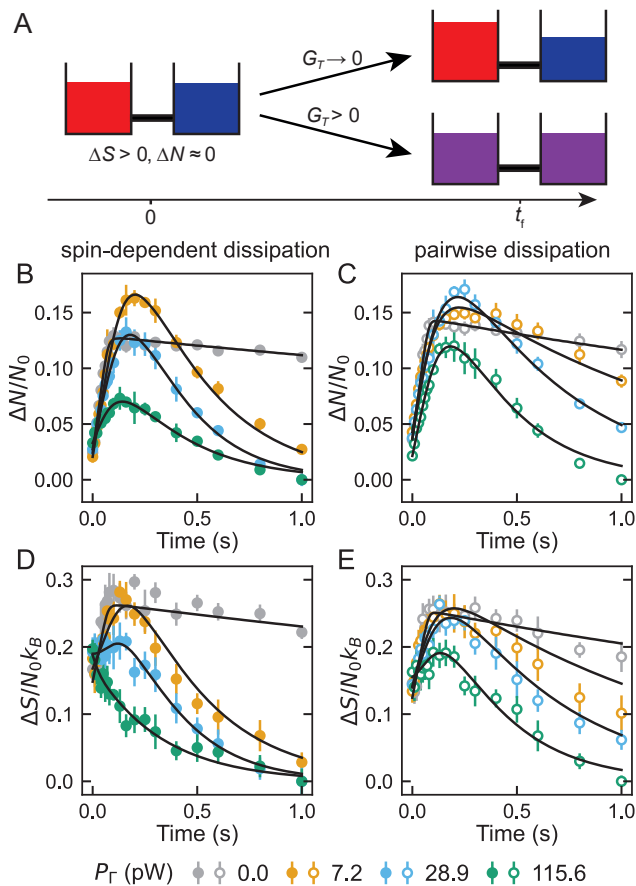


FIG. 2. **Coupled particle and thermal transport revealing entropy diffusion enhanced by both spin-dependent and pairwise dissipation.** System evolution in normalized particle (B,C) and entropy (D,E) imbalances starting from a pure entropy imbalance (illustrated in A), with spin-dependent (B,D) and pairwise dissipation (C,E). The initial advective response is enhanced by weak dissipation (e.g., orange circles in B). The dissipation strength is quantified by the optical power of the dissipation beam, P_T . The diffusion timescale after the initial response decreases monotonically with increasing P_T . Markers (error bars) correspond to averages (standard deviations) over 5 repetitions. Solid curves are fit to the phenomenological model (see text).

is varied up to $P_{\max} = 116(2)$ pW or $I_{\max} = 44(2)$ W/m² at the center of the beam, corresponding to a maximal $\Gamma_{\downarrow} = 93(2)$ ms⁻¹ for spin-dependent dissipation. Due to the locality of the dissipation, neither method induces substantial heating to the reservoirs (See SI [42]).

In the first set of measurements we focus on coupled entropy and particle transport. In order to observe both the advective and diffusive responses, we start the experiment with no particle imbalance $\Delta N = 0$ but an entropy imbalance $\Delta S > 0$ (Fig. 2A). The system dynamics are analogous to the Seebeck effect in thermoelectric materials where a current is induced by a temperature difference. The advective current in our system dominates the initial response. It is driven by both the chemical po-

tential bias $\Delta\mu$ and temperature bias ΔT , with a total thermodynamic force $\Delta\mu + \alpha_c \Delta T$, where α_c is the Seebeck coefficient, i.e., the transported entropy per particle. After this driving force is balanced with a remaining temperature imbalance $\Delta T > 0$, thermal diffusion provides a way for the system to fully relax to equilibrium (Fig. 2A). The timescale of the diffusive relaxation is characterized by the thermal conductance G_T as the diffusive entropy current responds linearly to ΔT .

In the absence of dissipation, the particle- and entropy-current response to $\Delta\mu$ and ΔT is highly nonlinear as observed previously [27, 33]. This leads to a highly non-exponential rise in both ΔN and ΔS (normalized by $N(t=0) \equiv N_0$, gray circles in Fig. 2B–E) and a sudden halt, when the advective response is balanced, followed by a very slow decay. The final state resembles a non-equilibrium steady state [27, 34] in which the thermal diffusion is negligible. In contrast, by applying either type of dissipation (in the order of increasing strength: orange, blue, and green circles in Fig. 2B–E), the initial response is slightly slower but the following timescale of diffusion becomes much faster, almost relaxing the system to equilibrium within 1 s. Notably, dissipation qualitatively reduces the nonlinear nature of the advective response leading to a smoother evolution of ΔN and ΔS .

In order to quantify the changes in advection and diffusion with dissipation, we fit the phenomenological model developed in Ref. [27] for closed systems, based on the theory of generalized gradient dynamics [46], which is a generalization of Onsager’s principle of irreversible processes. The model accommodates a *nonlinear* advective current (particle and entropy) and a linear diffusive current (entropy):

$$\begin{aligned} I_N &= I_{\text{exc}} \tanh\left(\frac{\Delta\mu + \alpha_c \Delta T}{\sigma}\right) \\ I_S &= \alpha_c I_N + G_T \Delta T / T, \end{aligned} \quad (1)$$

where I_{exc} is the “excess” current the system reaches after saturating the nonlinearity (biases exceeding σ) [27, 36] and σ is an energy scale that determines the nonlinearity of the current response. Combining Eq. 1 with the linear reservoir response [38, 42], the dynamics of the reservoirs in the $(\Delta N, \Delta S)$ space can be fully described. Although the phenomenological model does not explicitly include losses, we find that the model can well fit the data with dissipation, when I_N and I_S represent the *apparent* currents: $I_N = (-1/2) d\Delta N/dt$ and $I_S = (-1/2) d\Delta S/dt$. The effect of the dissipation is encapsulated in changes of the transport coefficients such as I_{exc} , σ , α_c and G_T . The fits for varying dissipation strength are shown as solid curves in Fig. 2B–E. They all share the same reservoir response coefficients so the fitted transport coefficients can reveal qualitative changes of the two transport modes. We will discuss these results further below in Fig. 4.

The enhancement of the “Seebeck” response—maximal ΔN reached—for weak dissipation strength (orange data in Fig. 2B, orange and blue data in Fig. 2C) stems from a change of the energy dependence of transport due to

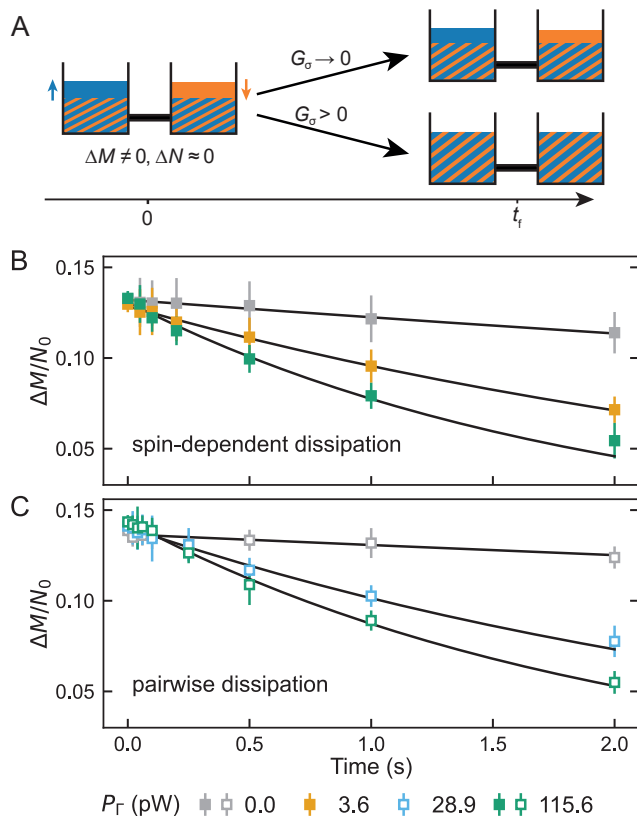


FIG. 3. **Spin diffusion between superfluid reservoirs enhanced by both spin-dependent and pairwise dissipation.** (A) Sketch of the initial $\Delta M \neq 0$, $\Delta N \approx 0$ and possible final states of the system with and without spin diffusion. (B) The relative magnetization $\Delta M/N_0$, plotted as a function of time, relaxes faster with increasing spin-dependent dissipation (from gray to green). (C) Applying pairwise dissipation in the quasi-1D junction also leads to decay of the relative magnetization. Solid black lines are fits to exponential decays. Markers (error bars) correspond to averages (standard deviations) over 5 repetitions.

dissipation. The microscopic mechanism is yet to be fully understood. Nevertheless, within the framework of our phenomenological model, this phenomenon can result from a 10% increase of $\alpha_r - \alpha_c$ by dissipation as shown in the fitted results [42], where $\alpha_r = (\partial S/\partial N)_T$ is the “entropy per particle” in order to keep the reservoir’s temperature [38]. Both α_c and α_r could be affected by dissipation. A possible scenario is an increase of α_r compared to α_c due to residual heating or dissipation preferentially removing low energy atoms, reducing the local degeneracy. As degeneracy goes down, α_r always increases.

In the second set of measurements we explore the effect of dissipation on spin transport through the junction. In contrast to the advective entropy current, the spin current I_M responds linearly to an applied spin bias $\Delta b = (\Delta\mu_\uparrow - \Delta\mu_\downarrow)/2$, such that $I_M = G_\sigma \Delta b$ where G_σ is the spin conductance. Fig. 3A illustrates the ini-

tial condition and possible final conditions in the system with high and low G_σ . The initial state is prepared to have a pure magnetization imbalance $\Delta M_0 = M_L - M_R \neq 0$, ($M_i = N_{i,\uparrow} - N_{i,\downarrow}$) and almost no initial particle or entropy imbalance $\Delta N_0 \approx \Delta S_0 \approx 0$. The subsequent relative magnetization $\Delta M(t)/N_0$ dynamics are displayed in Fig. 3B,C for a selection of measured dissipation strengths. Without dissipation (gray squares) the magnetization imbalance is hardly relaxing within the explored timescale (2s), indicating spin-insulating behavior in line with previous results [24]. Introducing spin-dependent dissipation (Fig. 3B) inside the junction leads to a faster spin relaxation, approaching equilibrium within the experimental timescale. Pairwise dissipation (Fig. 3C) also leads to similar enhanced spin diffusion. In order to quantify the change of spin diffusion with dissipation an offset-free exponential decay is fitted (solid lines in Fig. 3B-C). The spin conductance G_σ is calculated from the fitted decay time constant [24].

We now examine how the entropy and spin diffusion scales with dissipation strength. Are they enhanced indefinitely as the dissipation increases or reaching certain limit? The fitted transport characteristics versus dissipation strength are summarized in Fig. 4. Figure 4A shows the initial loss current $I_\Gamma(0) = \gamma_N N_0/2$ from all experiments, obtained from an exponential fit to the total atom number $N(t) = N_0 e^{-\gamma_N t}$. The loss current shows a trend of saturation as a function of the dissipation power P_Γ . Spin-dependent dissipation leads to higher losses at low P_Γ and saturates faster compared to pairwise dissipation. Fig. 4B shows the initial particle current $I_N(0)$ from the entropy transport experiment (Fig. 2), obtained from a linear fit to the initial evolution of ΔN [42]. Similar to previous results [29] we find that dissipation decreases the particle current, but it remains much higher than the normal current expected in a non-interacting 1D junction $I_{n0} = 2n_m \Delta\mu/h$ (dotted horizontal line), where n_m is the number of occupied transverse modes in the channel. The observed current $I_N = -(\dot{N}_L - \dot{N}_R)/2$ can in principle arise purely from asymmetric losses, so we provide a lower bound for the *conserved* current I^{cons} —atoms transported through the junction without being lost. By writing $\dot{N}_{L/R} = \mp I^{\text{cons}} - I_{L/R}^{\text{loss}}$, where $I_{L/R}^{\text{loss}}$ is the loss current from each reservoir, we have $I_N = I^{\text{cons}} + (I_L^{\text{loss}} - I_R^{\text{loss}})/2$ and $I_\Gamma = (I_L^{\text{loss}} + I_R^{\text{loss}})/2$. The lower bound for $I^{\text{cons}}(0)$ is given by $I_N(0) - I_\Gamma(0)$, assuming the unlikely scenario where the lost atoms all come from one reservoir. These bounds are shown in the same line shape as $I_N(0)$ in lighter colors.

Figure 4C shows the normalized thermal conductance \tilde{G}_T (circles) as a function of dissipation power P_Γ . They are obtained from fitting the phenomenological model to data from the entropy transport experiment (Fig. 2) [27, 42]. Moreover, Fig. 4C contains the normalized spin conductance \tilde{G}_σ (squares, from Fig. 3) from the spin transport experiment. Both conductances are normalized by their non-interacting expectation in a non-dissipative 1D junction, i.e., $G_{T,0} = 2n_m \pi^2 k_B^2 T/3h$ and

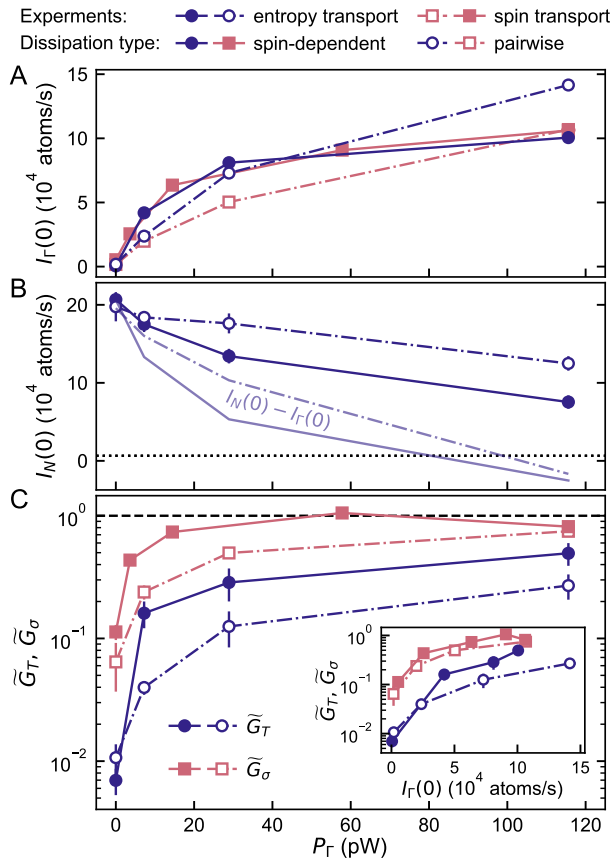


FIG. 4. **Extracting thermal and spin conductances versus dissipation strength, showing their saturation to values for non-interacting fermions.** (A) The average loss current $I_r(0)$ from each reservoir is shown as a function of dissipation power P_T . Navy circles (pink squares) correspond to the entropy (spin) transport experiment, and filled (open) symbols correspond to spin-dependent (pairwise) dissipation. Transport coefficients are obtained from fits to the dynamics observed in the entropy transport (circles) and spin transport (squares) measurements, displayed in Fig. 2 and Fig. 3, respectively. (B) Initial particle current $I_N(0)$. The dotted horizontal line indicates the expected particle current in a non-interacting, non-dissipative ballistic 1D junction. The lines in lighter color are the lower bounds for the conserved current, given by $I_N(0) - I_r(0)$ (see text). (C) The normalized spin conductance \tilde{G}_σ (squares) and thermal conductance \tilde{G}_T (circles) are plotted versus the dissipation strength and versus the initial loss current (inset). The unity value (dashed horizontal line) corresponds to a non-interacting ballistic 1D junction without dissipation. Error bars correspond to standard errors from the fit. They are smaller than the marker size if not visible.

$G_{\sigma,0} = 2n_m/h$, such that $\tilde{G}_T, \tilde{G}_\sigma = 1$ correspond to the non-interacting values (dashed horizontal line). The factor of 2 accounts for the two spins. We find that both dissipation types induce a sharp increase of more than one order of magnitude in spin conductance and almost two orders of magnitude in thermal conductance. Interest-

ingly, both conductances seem to approach their values in the non-interacting regime without dissipation, which is a quantum limit given by the quantization of transverse modes in the 1D channel. These conductances are much higher than the apparent transport purely arising from atom loss [42], so the enhanced diffusion is not an artefact of losses. The same experiments have been performed with different transverse confinements ν_x hence different n_m (within the quasi-1D regime), giving similar results when normalized by n_m , see SI [42]. Possible uncertainties in the fitting of G_T are also discussed in SI [42]. We can further compare the two types of dissipation by replotting the conductances versus the loss current (inset of Fig. 4C). In this regard, the two mechanisms lead to similar spin and thermal diffusion for a given particle loss rate, with the pairwise dissipation being slightly less “destructive” to the superfluid junction. This difference, albeit small, agrees with the weaker suppression of particle current by pairwise loss (Fig. 4B), and could have the following origin. While the pairwise dissipation reduces the pairing field which could be replenished by the superfluid reservoirs, the spin-dependent dissipation creates an unpaired quasi-particle excitation above the superfluid gap and is harder to remove. At strong dissipation, both types of dissipation seem to approach the same limit. Although the microscopic mechanism of this limited transport remains unclear, it is conceivable that the quantized conductance in 1D systems holds as a general limit for all types of excitations obeying the Pauli principle. In contrast to the non-interacting system where strong dissipation explored here would significantly reduce the quantized conductance [28], our strongly interacting system is reaching the non-dissipative, quantized conductance limit.

In summary, we have studied the effects of spin-dependent and pairwise dissipation on thermal and spin transport between two superfluids connected by a quasi-1D ballistic junction. We have found that dissipation leads to a remarkable increase in thermal and spin diffusion, and the conductances approach the quantum limited, non-interacting values. This suggests that the pairing gap that initially suppresses thermal excitation is destroyed by dissipation. However, this picture cannot fully explain the observation that the superfluid-assisted particle current is largely preserved, possibly due to the strong attractive interactions [29, 47]. Our observations call for a microscopic description of the system that might be crucial to understanding the nature of the quantum limited transport in the strongly-interacting and strongly-dissipative system. Moreover, the sharp increase of thermal and spin conductances at weak dissipation as well as the enhanced “Seebeck” response demonstrate a possibility to dissipatively control the “thermoelectric” and spin transport in a superfluid junction. These mechanisms may shed light on the design of functional thermoelectric or spintronic devices.

ACKNOWLEDGMENTS

We thank Alexander Frank for his contributions to the electronics of the experiment. We are thankful for inspiring discussions with Sebastian Diehl, Alex Gómez

Salvador, Yi-Fan Qu and Eugene Demler. We acknowledge the Swiss National Science Foundation (Grants No. 212168, UeM019-5.1, and TMAG-2.209376) and European Research Council advanced grant TransQ (Grant No. 742579) for funding.

-
- [1] P. B. Patel, Z. Yan, B. Mukherjee, R. J. Fletcher, J. Struck, and M. W. Zwierlein, Universal sound diffusion in a strongly interacting Fermi gas, *Science* **370**, 1222 (2020).
- [2] X. Li, X. Luo, S. Wang, K. Xie, X.-P. Liu, H. Hu, Y.-A. Chen, X.-C. Yao, and J.-W. Pan, Second sound attenuation near quantum criticality, *Science* **375**, 528 (2022).
- [3] Z. Yan, P. B. Patel, B. Mukherjee, C. J. Vale, R. J. Fletcher, and M. W. Zwierlein, Thermography of the superfluid transition in a strongly interacting Fermi gas, *Science* **383**, 629 (2024).
- [4] A. Sommer, M. Ku, G. Roati, and M. W. Zwierlein, Universal spin transport in a strongly interacting Fermi gas, *Nature* **472**, 201 (2011).
- [5] C. Luciuk, S. Smale, F. Böttcher, H. Sharum, B. A. Olsen, S. Trotzky, T. Enss, and J. H. Thywissen, Observation of Quantum-Limited Spin Transport in Strongly Interacting Two-Dimensional Fermi Gases, *Physical Review Letters* **118**, 130405 (2017).
- [6] C. Cao, E. Elliott, J. Joseph, H. Wu, J. Petricka, T. Schäfer, and J. E. Thomas, Universal Quantum Viscosity in a Unitary Fermi Gas, *Science* **331**, 58 (2011).
- [7] X. Wang, X. Li, I. Arakelyan, and J. E. Thomas, Hydrodynamic Relaxation in a Strongly Interacting Fermi Gas, *Physical Review Letters* **128**, 090402 (2022).
- [8] A. Adams, L. D. Carr, T. Schäfer, P. Steinberg, and J. E. Thomas, Strongly correlated quantum fluids: ultracold quantum gases, quantum chromodynamic plasmas and holographic duality, *New Journal of Physics* **14**, 115009 (2012).
- [9] H. Guo, D. Wulin, C.-C. Chien, and K. Levin, Perfect fluids and bad metals: insights from ultracold Fermi gases, *New Journal of Physics* **13**, 075011 (2011).
- [10] S. A. Hartnoll and A. P. Mackenzie, *Colloquium*: Planckian dissipation in metals, *Reviews of Modern Physics* **94**, 041002 (2022).
- [11] X. Han and S. A. Hartnoll, Locality Bound for Dissipative Quantum Transport, *Physical Review Letters* **121**, 170601 (2018).
- [12] G. Barontini, R. Labouvie, F. Stubenrauch, A. Vogler, V. Guarrera, and H. Ott, Controlling the Dynamics of an Open Many-Body Quantum System with Localized Dissipation, *Physical Review Letters* **110**, 035302 (2013).
- [13] H. Fröml, C. Muckel, C. Kollath, A. Chiocchetta, and S. Diehl, Ultracold quantum wires with localized losses: Many-body quantum Zeno effect, *Physical Review B* **101**, 144301 (2020).
- [14] K. Behnia, D. Jaccard, and J. Flouquet, On the thermoelectricity of correlated electrons in the zero-temperature limit, *Journal of Physics: Condensed Matter* **16**, 5187 (2004).
- [15] R. A. Davison, W. Fu, A. Georges, Y. Gu, K. Jensen, and S. Sachdev, Thermoelectric transport in disordered metals without quasiparticles: The Sachdev-Ye-Kitaev models and holography, *Physical Review B* **95**, 155131 (2017).
- [16] Y. Sekino, H. Tajima, and S. Uchino, Mesoscopic spin transport between strongly interacting Fermi gases, *Physical Review Research* **2**, 023152 (2020).
- [17] G. B. Partridge, K. E. Strecker, R. I. Kamar, M. W. Jack, and R. G. Hulet, Molecular Probe of Pairing in the BEC-BCS Crossover, *Physical Review Letters* **95**, 020404 (2005).
- [18] X.-P. Liu, X.-C. Yao, H.-Z. Chen, X.-Q. Wang, Y.-X. Wang, Y.-A. Chen, Q. Chen, K. Levin, and J.-W. Pan, Observation of the density dependence of the closed-channel fraction of a ^6Li superfluid, *National Science Review*, nwab226 (2021).
- [19] R. Labouvie, B. Santra, S. Heun, and H. Ott, Bistability in a Driven-Dissipative Superfluid, *Physical Review Letters* **116**, 235302 (2016).
- [20] T. Tomita, S. Nakajima, I. Danshita, Y. Takasu, and Y. Takahashi, Observation of the Mott insulator to superfluid crossover of a driven-dissipative Bose-Hubbard system, *Science Advances* **3**, e1701513 (2017).
- [21] N. Dogra, M. Landini, K. Kroeger, L. Hruby, T. Donner, and T. Esslinger, Dissipation-induced structural instability and chiral dynamics in a quantum gas, *Science* **366**, 1496 (2019).
- [22] R. Bouganne, M. Bosch Aguilera, A. Ghermaoui, J. Beugnon, and F. Gerbier, Anomalous decay of coherence in a dissipative many-body system, *Nature Physics* **16**, 21 (2020).
- [23] D. Dreon, A. Baumgärtner, X. Li, S. Hertlein, T. Esslinger, and T. Donner, Self-oscillating pump in a topological dissipative atom-cavity system, *Nature* **608**, 494 (2022).
- [24] S. Krinner, M. Lebrat, D. Husmann, C. Grenier, J.-P. Brantut, and T. Esslinger, Mapping out spin and particle conductances in a quantum point contact, *Proceedings of the National Academy of Sciences* **113**, 8144 (2016).
- [25] G. Valtolina, F. Scazza, A. Amico, A. Burchianti, A. Recati, T. Enss, M. Inguscio, M. Zaccanti, and G. Roati, Exploring the ferromagnetic behaviour of a repulsive Fermi gas through spin dynamics, *Nature Physics* **13**, 704 (2017).
- [26] L. H. Dogra, G. Martirosyan, T. A. Hilker, J. A. P. Glidden, J. Etrych, A. Cao, C. Eigen, R. P. Smith, and Z. Hadzibabic, Universal equation of state for wave turbulence in a quantum gas, *Nature* **620**, 521 (2023).
- [27] P. Fabritius, J. Mohan, M. Talebi, S. Wili, W. Zwirger, M.-Z. Huang, and T. Esslinger, Irreversible entropy transport enhanced by fermionic superfluidity, *Nature Physics* **20**, 1091 (2024).
- [28] L. Corman, P. Fabritius, S. Häusler, J. Mohan, L. H. Dogra, D. Husmann, M. Lebrat, and T. Esslinger, Quantized conductance through a dissipative atomic point contact, *Physical Review A* **100**, 053605 (2019).

- [29] M.-Z. Huang, J. Mohan, A.-M. Visuri, P. Fabritius, M. Talebi, S. Wili, S. Uchino, T. Giamarchi, and T. Esslinger, Superfluid Signatures in a Dissipative Quantum Point Contact, *Physical Review Letters* **130**, 200404 (2023).
- [30] A.-M. Visuri, J. Mohan, S. Uchino, M.-Z. Huang, T. Esslinger, and T. Giamarchi, DC transport in a dissipative superconducting quantum point contact, *Physical Review Research* **5**, 033095 (2023).
- [31] W. Zwerger, ed., *The BCS-BEC Crossover and the Unitary Fermi Gas*, Lecture notes in physics No. 836 (Springer, Heidelberg, 2012).
- [32] A. J. Leggett, *Quantum liquids: Bose condensation and Cooper pairing in condensed-matter systems*, Oxford graduate texts (Oxford University Press, Oxford ; New York, 2006).
- [33] D. Husmann, S. Uchino, S. Krinner, M. Lebrat, T. Giamarchi, T. Esslinger, and J.-P. Brantut, Connecting strongly correlated superfluids by a quantum point contact, *Science* **350**, 1498 (2015).
- [34] D. Husmann, M. Lebrat, S. Häusler, J.-P. Brantut, L. Cormann, and T. Esslinger, Breakdown of the Wiedemann–Franz law in a unitary Fermi gas, *Proceedings of the National Academy of Sciences* , 201803336 (2018).
- [35] S. S. Pershoguba and L. I. Glazman, Thermopower and thermal conductance of a superconducting quantum point contact, *Physical Review B* **99**, 134514 (2019).
- [36] J. C. Cuevas, A. Martín-Rodero, and A. L. Yeyati, Hamiltonian approach to the transport properties of superconducting quantum point contacts, *Physical Review B* **54**, 7366 (1996).
- [37] E. Scheer, P. Joyez, D. Esteve, C. Urbina, and M. H. Devoret, Conduction Channel Transmissions of Atomic-Size Aluminum Contacts, *Physical Review Letters* **78**, 3535 (1997).
- [38] C. Grenier, C. Kollath, and A. Georges, Thermoelectric transport and Peltier cooling of cold atomic gases, *Comptes Rendus Physique* **17**, 1161 (2016).
- [39] S. Krinner, D. Stadler, D. Husmann, J.-P. Brantut, and T. Esslinger, Observation of quantized conductance in neutral matter, *Nature* **517**, 64 (2014).
- [40] S. Datta, *Electronic transport in mesoscopic systems* (Cambridge University Press, Cambridge; New York, 1995).
- [41] K. Damle and S. Sachdev, Nonzero-temperature transport near quantum critical points, *Physical Review B* **56**, 8714 (1997).
- [42] See Supplemental information on experimental procedures and data analysis.
- [43] F. Werner, L. Tarruell, and Y. Castin, Number of closed-channel molecules in the BEC-BCS crossover, *The European Physical Journal B* **68**, 401 (2009).
- [44] J. Wang, X.-J. Liu, and H. Hu, Photoexcitation measurement of Tan’s contact for a strongly interacting Fermi gas, *Physical Review A* **104**, 063309 (2021).
- [45] M. Jäger and J. H. Denschlag, *Precise photoexcitation measurement of Tan’s contact in the entire BCS-BEC crossover* (2023), arXiv:2309.17305 [cond-mat].
- [46] M. Pavelka, V. Klika, and M. Grmela, *Multiscale thermodynamics: introduction to GENERIC* (De Gruyter, Berlin ; Boston, 2018).
- [47] M. Gievers, T. Müller, H. Fröml, S. Diehl, and A. Chiocchetta, Quantum wires with local particle loss: Transport manifestations of fluctuation-induced effects, *Physical Review B* **110**, 205419 (2024).

SUPPLEMENTAL INFORMATION

S1. EXPERIMENTAL DETAILS

A. Preparation

The transport geometry is created by intersecting two repulsive TEM_{01} like laser beams (along x and z) at the center of a cigar-shaped harmonic trap, separating it into two half-harmonic reservoirs connected by a channel. The harmonic trapping frequencies are $\nu_x = 171(1)$ Hz, $\nu_y = 28.3(1)$ Hz and $\nu_z = 164(1)$ Hz. The channel forming beam along x (“lightsheet”) has a waist of $w_{y,\text{LS}} \approx 30.2 \mu\text{m}$ along the transport direction y , forming a 2D region in the $x-y$ plane. Within this 2D region, the waist of the other channel forming beam along z determines the length of the 1D channel, $w_{y,\text{ch}} \approx 6.8 \mu\text{m}$ (here the beam waists w are defined as the $1/e^2$ beam radius). An attractive, circular, ($w_g \approx 31.8 \mu\text{m}$) “gate” beam, propagating along z , is centered on the channel to control the local potential $V_g/k_B = 2.17(10) \mu\text{K}$ at the channel contacts. A fast CCD camera is used to sequentially image the atomic clouds of each spin state after every experimental run. The first absorption image is taken of state $|\downarrow\rangle$ which leads to off-resonant photon scattering of state $|\uparrow\rangle$ that perturbs the shape of the cloud. This results in a slight overestimation $\sim 5\%$ of the entropy of $|\uparrow\rangle$ but we do not apply any correction for simplicity and being conservative. More details on the preparation and thermometry of the system can be found in our previous work [27].

B. Spin-dependent and pairwise dissipation

A laser beam resonant at $|\downarrow\rangle \equiv |2S_{1/2}, m_J = -1/2, m_I = 1\rangle \rightarrow |2P_{3/2}, m_J = 3/2, m_I = 0\rangle$ transition, with a waist of $w = 1.3(1) \mu\text{m}$ is projected onto the channel (along z) using a digital micro-mirror device for aberration correction. The used transition optically pumps atoms from the lowest hyperfine-state $|\downarrow\rangle$ to an auxiliary hyperfine state $|5\rangle \equiv |2S_{1/2}, m_J = 1/2, m_I = 0\rangle$. This state is neither trapped, nor does it interact with $|\downarrow\rangle$ or $|\uparrow\rangle \equiv |2S_{1/2}, m_J = -1/2, m_I = -1\rangle$, such that atoms which scattered a photon leave the trap unimpeded. We calibrate the power and the intensity of the beam using both a powermeter and a camera. Using the calibration we can calculate the atom-photon scattering rate which is $\Gamma_{\downarrow}/P_{\Gamma} = 0.80(1) \text{ms}^{-1}/\text{pW}$. Generally, the intensities used in this paper are far below the saturation intensity of the transition $I_{\text{sat}} = 8.7 \text{kW}/\text{m}^2$.

Pairwise dissipation is engineered using the same beam, by tuning its frequency to a molecular photoassociation resonance (similar to Ref. [17, 44]) which is 851 MHz blue detuned from the center of the D_2 line. Since we are not able to calculate the photoassociation absorption rate *ab initio* we use the dissipation power as the main experimental variable. We confirm that atoms

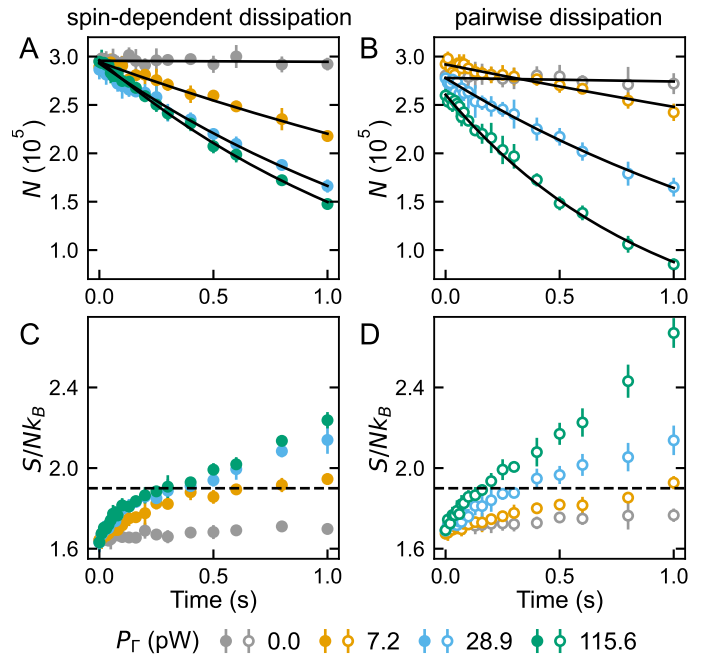


FIG. S1. **Atom loss and heating with dissipation.** Data are from the entropy transport experiment (Fig. 2). Data for the spin transport experiment are similar and not shown. (A,B) Total atom number as a function of time. The solid lines are fits to exponential decay. (C,D) The entropy per particle increases over time mostly due to atom losses rather than heating, as temperatures remain almost the same (see Tab. S1). The majority of data points is still below the superfluid transition $s_c \approx 1.9$ (dashed line) in our reservoirs.

are lost in pairs by varying the spin polarization of the gas, finding that atom losses are negligible in a fully spin polarized cloud. Moreover, we find that the associated molecular state leaves the trap without additional interactions with the cloud, namely without significant heating in the reservoirs.

C. Heating and atom loss

The observed initial and final thermodynamic properties of the reservoirs are summarized in Tab. S1 for all experiments discussed in the main text. The dynamics of atom number N and entropy per particle S/N in the entropy transport experiment are displayed in Fig. S1. We find that the engineered dissipation does not lead to significant heating, $T(t=0) \approx T(t=1 \text{s})$. The observed reduction of degeneracy stems predominantly from the atom loss. Importantly, the majority of the data points is still below the critical entropy per particle $s_c/k_B \approx 1.9$ [27], suggesting that heating the reservoirs beyond the critical point is not responsible for most of the observed changes in the transport dynamics. The observed enhanced diffusion is already significant for the smallest dissipation where the reservoirs stay superfluid

| | | |
|-----------|------------------------|----------------------|
| A | $t_i = 0$ s | $t_f = 1$ s |
| S/Nk_B | 1.65(3) | 2.6(3) |
| N | $2.86(15) \times 10^5$ | $1.0(3) \times 10^5$ |
| μ/k_B | 235(5) nK | 113(30) nK |
| B | $t_i = 0$ s | $t_f = 1$ s |
| S/Nk_B | 1.75(4) | 2.27(5) |
| N | $2.9(2) \times 10^5$ | $1.4(1) \times 10^5$ |
| μ/k_B | 232(7) nK | 152(7) nK |

TABLE S1. **Overview of initial and final thermodynamic quantities.** Table A shows the values measured for the entropy transport experiment (see Fig. 2 and Fig. S1). Table B shows the quantities for the spin transport experiment (see Fig. 3). For the latter, although the data are taken up to $t = 2$ s, we show here properties at $t_f = 1$ s for comparison with (A). The initial properties of the reservoirs at t_i are averages over all datasets in the corresponding experiment. The final properties at t_f are calculated for the datasets with the strongest dissipation $P_\Gamma = 115.6$ pW, averaging the spin-dependent and pairwise dissipation.

throughout the full transport dynamics. Moreover, the low thermal conductance in the absence of dissipation has been observed previously [34] at a degeneracy of $q = \mu/k_B T = 1.5(2)$ which is comparable to the lowest degeneracy measured here $q = 1.2(3)$ (see Tab. S1A). Thus even above the superfluid transition the strong attractive interactions and the local pairing gap [24, 34] (enhanced by the gate potential) prevent spin and thermal diffusion. The total local potential around the channel $V_{\text{tot}} = V_g + \mu$ is weakly affected by dissipation since it is dominated by the gate potential $V_g \gg \mu$. This means that the number of occupied transport modes n_m is almost constant during transport. For $\nu_x = 10.9$ kHz the number of thermally occupied modes (assuming Fermi-Dirac distribution) reduces from $n_m(t_i) \approx 3.1$ to $n_m(t_f) \approx 2.7$, using the thermodynamic quantities in Tab. S1A.

S2. FITTING PROCEDURE

A. Atom number fit

The overall atom loss rate is determined from a fit of the atom number evolution $N(t)$ shown in Fig. S1A,B with an exponential decay function given by

$$N_{\text{fit}}(t) = N_0 e^{-\gamma_N t}. \quad (\text{S2})$$

The initial value N_0 and the loss rate γ_N are fitted using the least-squares method. The sum of squared residuals is calculated from the mean and weighted by the inverse of the standard deviation of each measured $N(t)$. The average loss current from each reservoir I_Γ is then defined as $I_\Gamma(t) = -\dot{N}(t)/2 = \gamma_N N(t)/2$ such that

$$I_\Gamma(0) = \gamma_N N_0/2. \quad (\text{S3})$$

B. Magnetization imbalance fit

The spin conductance is determined from a fit of the magnetization imbalance evolution $\Delta M(t)$ with an exponential decay function given by

$$\Delta M_{\text{fit}}(t) = \Delta M_0 e^{-t/\tau_\sigma}. \quad (\text{S4})$$

The initial imbalance ΔM_0 and the timescale of spin transport τ_σ are fitted using the least-squares method. The spin conductance G_σ in the spin-degenerate system is then given by

$$G_\sigma = \frac{\chi}{4\tau_\sigma}, \quad (\text{S5})$$

where the spin susceptibility is defined as $\chi = 2 \frac{\partial(N_\uparrow - N_\downarrow)}{\partial(\mu_\uparrow - \mu_\downarrow)}$. The spin susceptibility is calculated from the initial ($t = 0$) atom number, temperature and magnetization. We did not find an appreciable difference when replacing the initial thermodynamic quantities by the average values over the full transport time. The spin conductance in the non-interacting, non-dissipative system for a ballistic 1D junction is $G_{\sigma,0} = 2n_m/h$ [40].

C. Phenomenological model fit

The differential equations obtained from the phenomenological model (1) are valid for the spin-degenerate system, where the reservoir response coefficients are calculated for the full-harmonic reservoirs (both spins in both reservoirs), for more detail see the Supplementary Material of Ref. [27]. The equations we use for the fit of the dynamics describing particle and entropy transport are given by

$$-\frac{1}{2} \frac{d\Delta N(t)}{dt} = I_{\text{exc}} \tanh\left(\frac{\Delta\mu + \alpha_c \Delta T}{\sigma}\right), \quad (\text{S6})$$

$$-\frac{1}{2} \frac{d\Delta S(t)}{dt} = -\frac{\alpha_c}{2} \frac{d\Delta N(t)}{dt} + G_T \frac{\Delta T}{T}. \quad (\text{S7})$$

The reservoir response is given by

$$\Delta\mu = \frac{(\ell_r + \alpha_r^2)\Delta N - \alpha_r \Delta S}{\ell_r \kappa/2}, \quad (\text{S8})$$

$$\Delta T = \frac{-\alpha_r \Delta N + \Delta S}{\ell_r \kappa/2}, \quad (\text{S9})$$

where $\kappa = (\partial N/\partial \mu)_T$ is the compressibility, $\alpha_r = (1/\kappa)(\partial S/\partial \mu)_T$ is the dilatation coefficient, and $\ell_r = C_N/T\kappa$, with $C_N = T(\partial S/\partial T)_N$, is the ‘‘Lorenz number’’ of the reservoirs [38]. The equations are integrated numerically in order to fit the measured entropy and atom number imbalances. We reduce the fluctuations in the data of $\Delta N(t)$ and $\Delta S(t)$ by multiplying the relative imbalances $\Delta N(t)/N(t)$ and $\Delta S(t)/N(t)$ from each experimental realization with the fitted atom-number $N_{\text{fit}}(t)$ (Eq. S2). The reservoir response coefficients are not fitted

directly, but the coefficients computed via the equation of state (EoS) are multiplied by a scaling factor which is fitted to account for fluctuations in atom number and temperature between datasets:

$$\alpha_r = \alpha_s \alpha_{\text{EoS}}, \quad \ell_r = \ell_s \ell_{\text{EoS}},$$

where the indices stand for: s – scale, EoS – computed from EoS. The reservoir coefficients are calculated using the initial atom number and entropy. The initial values $\Delta N(0)$ and $\Delta S(0)$ are fixed from the data. Initial parameters for the thermal conductance G_T are determined from a diffusive timescale τ_d , obtained from an exponential fit starting at the turning point (maximum ΔN) of the particle imbalance evolution (Fig. 2B,C). They are related, in the limit that the advective transport timescale is much shorter than the diffusive timescale, by

$$G_T \approx \frac{T\kappa(\ell_r + (\alpha_c - \alpha_r)^2)}{4\tau_d}. \quad (\text{S10})$$

The fit parameters are listed in Table S2. Only the Seebeck coefficient α_c , the thermal conductance G_T and the nonlinearity coefficient σ are fitted individually for each dataset. The scaling factors of the Lorentz number ℓ_s and dilatation coefficient α_s of the reservoirs are fitted simultaneously for all datasets (varying the strength and type of dissipation, as well as transverse confinement ν_x of the channel). Note that both α_c and α_r could be affected by dissipation as we discussed in the main text. However, only $\alpha_c - \alpha_r$ is relevant for the dynamics so we made a choice to fix α_r among datasets in the fit to limit the degrees of freedom. The fit result gives $\ell_r/k_B^2 = 0.028(1)$ and $\alpha_r/k_B = 1.19(4)$.

Moreover, the compressibility κ is fixed to the computation from the EoS. The excess current I_{exc} is fixed from the initial current $I_N(0)$, which is determined from a linear fit to the initial particle imbalance evolution. The linear fit includes between 4 and 10 data points. Starting with 4 points the linear fit is repeated with increasing number of points until the reduced χ^2 is minimized. The residual sum of squares for minimization is a concatenation of deviations in ΔN and ΔS of all datasets, with weights given by the inverse averaged standard deviations of ΔN and ΔS respectively for each dataset. In addition to the 8 datasets shown in Fig. 2 (4 datasets per dissipation type) 16 more datasets (8 datasets per transverse confinement) are fitted simultaneously (Fig. S2). The auxiliary datasets were measured for confinement frequencies of $\nu_x = 9.5(2)$ kHz and $\nu_x = 8.0(2)$ kHz, within the quasi-1D regime. All datasets can be well described with the phenomenological model, reaching a goodness of fit parameter of reduced χ^2 of 0.65.

The excess current I_{exc} (fixed to initial apparent current $I_N(0)$ from data), Seebeck coefficient α_c , nonlinearity coefficient σ and normalized thermal conductance \tilde{G}_T for all datasets are shown in Fig. S2. We find that the results displayed in Fig. 4 are reproduced for various confinement frequencies and thus different number of occupied modes.

| | |
|---------------------------|--------------------------|
| fitted for each dataset | α_c, G_T, σ |
| shared among all datasets | ℓ_s, α_s |
| fixed | κ, I_{exc} |

TABLE S2. Fit parameters.

The obtained conductance is normalized with $G_{T,0} = 2n_m\pi^2k_B^2T/3h$ in Fig. 4C and Fig. S2D such that \tilde{G}_T is independent of temperature T . The number of occupied channel modes n_m is calculated from the Fermi-Dirac distribution of the reservoirs and the expected energy landscape of the channel, for more details see the Methods of Ref. [27].

The current I_{n0} for a non-interacting system shown in Fig. 4B (dotted horizontal line) is calculated assuming a chemical potential bias of $\Delta\mu = 50$ nK, which corresponds to the largest ΔN observed, and the number of modes given by n_m such that $I_{n0} = 2n_m\Delta\mu/h$. The initial currents displayed in Fig. S2C differ mostly due to the different number of occupied modes. In (E) we normalize the current by n_m , showing that the measured initial currents fall on top of each other without dissipation.

S3. COMPARISON OF SPIN-DEPENDENT AND PAIRWISE DISSIPATION

Figure S2E,F replot the initial particle current and the normalized thermal conductance \tilde{G}_T versus the initial loss current. Plotting them as functions of the loss current—equivalent to an overall loss rate—offers one way to compare the effects of spin-dependent (filled symbols) and pairwise dissipation (open symbols). We find that at an equivalent loss current, pairwise losses suppress the particle current less than spin-dependent losses. Likewise, pairwise losses enhance the thermal conductance less than spin-dependent losses. This shows that the nature of the dissipation plays a role in slowing down the particle transport and in enabling entropy diffusion. As mentioned in the main text, a possible mechanism is that particle current depends on the locally suppressed superfluid order and the timescale with which the order can be re-established via the reservoirs. In this picture pairwise losses, which act on the superfluid order parameter [17], can be directly replenished by the superfluid reservoirs. In contrast, the spin-dependent loss creates a local, unpaired quasi-particle excitation above the superfluid gap with excess energy that could be more destructive to the the superfluid order.

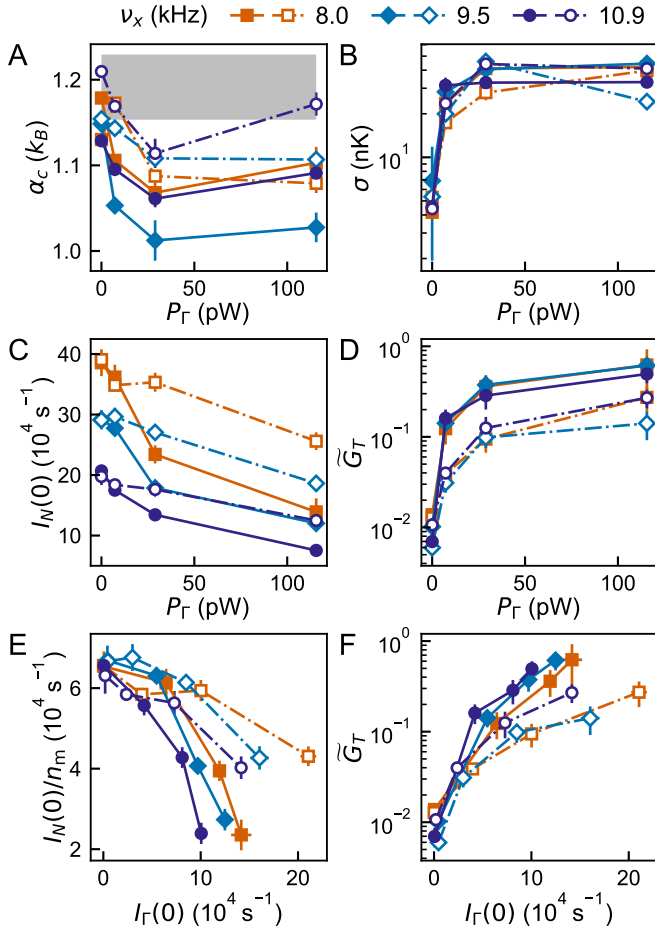


FIG. S2. **Fitted transport coefficients for extended datasets in the entropy transport experiment.** Filled (open) symbols again represent spin-dependent (pairwise) dissipation. The fitted Seebeck coefficient (A) as a function of dissipation beam power is slightly decreasing for weak dissipation. The gray bar represents the average fitted $\alpha_r = 1.19(4)$, showing that $\alpha_r - \alpha_c$ increases with weak dissipation. (B) The nonlinearity coefficient σ increases sharply with dissipation, indicating a more linear transport response. (C,D) Initial advective particle current $I_N(0)$ and normalized thermal conductance \tilde{G}_T versus dissipation strength. Errorbars are standard deviations from the least squares fit. Current and conductance of (C,D) are replotted in (E,F) versus the initial loss current on the horizontal axis. The initial currents (E) are also normalized by the number of transverse mode n_m . (E,F) serve to compare the two dissipation mechanisms, showing that pairwise dissipation generally has a weaker effect on transport for a given particle loss rate.

S4. DISCUSSION ON THE UNCERTAINTIES OF THE FITTED CONDUCTANCES

A. Thermal conductance

Since G_T results from a fit to the phenomenological model, it might be dependent on the fitted reservoir response coefficients. In particular, as noted previously [27]

the fitted ℓ_r strongly deviates from the theoretical value from the 3D EoS for harmonically trapped reservoirs, indicating that these response functions depend on details of the potential landscape.

It can be shown that within our phenomenological model, in the limit of small G_T (non-dissipative case), ℓ_r , α_c and α_r are constrained by the maximum ΔN reached after preparing an initial $\Delta S_0 > 0$ by

$$\Delta N_{\max} \approx \frac{\alpha_r - \alpha_c}{\ell_r + (\alpha_r - \alpha_c)^2} \Delta S_0. \quad (\text{S11})$$

In this limit, ℓ_r has a maximum value of $(\Delta S_0 / \Delta N_{\max})^2 / 4$ and $\alpha_r - \alpha_c \in (0, \Delta S_0 / \Delta N_{\max})$. The bounds of $\alpha_r - \alpha_c$ are approached when $\ell_r \rightarrow 0$. From Eq. S11 alone, $\alpha_r - \alpha_c$ could be either below or above $\Delta S_0 / (2\Delta N_{\max})$. However, we can put an upper bound for $\alpha_r < S/N$ based on physical arguments. $\alpha_r = (\partial S / \partial N)_T$ has the physical meaning of the entropy per particle when removing atoms from the reservoir through the channel while maintaining the temperature. At the center of the trap where the channel is connected, the entropy per particle is smaller than the average entropy per particle of the whole reservoir. This generally excludes the upper branch for $\alpha_r - \alpha_c > \Delta S_0 / (2\Delta N_{\max})$. Our fits do favor small $\alpha_r - \alpha_c$ in the regime where $\alpha_r - \alpha_c \approx (\Delta N_{\max} / \Delta S_0) \ell_r$.

Therefore, we can use $\alpha_r < S/N$ where S/N is from the non-dissipative data, α_c from the fitted entropy per particle of the advective mode in the absence of dissipation, and the independently fitted diffusive timescale τ_d (exponential decay after the initial response) to obtain an upper bound for G_T using Eq. S10 and Eq. S11,

$$G_T \approx \frac{T\kappa(\alpha_r - \alpha_c)\Delta S_0}{4\tau_d\Delta N_{\max}} < \frac{T\kappa(S_0/N_0 - \alpha_c)\Delta S_0}{4\tau_d\Delta N_{\max}}. \quad (\text{S12})$$

In Fig. S3 we plot the same \tilde{G}_T as in Fig. 4, with the corresponding upper bounds from Eq. S12 shown in the same lineshape with a lighter color. These bounds are also very close to 1, that is, the non-interacting limit without dissipation.

On the other hand, we plot the equivalent thermal conductance from an apparent transport due to pure losses from both reservoirs (black lines in the corresponding lineshapes below the data). That is, without any real transport, ΔN will decay exponentially with rate γ_N if each reservoir decays exponentially at rate γ_N . However, this scenario would give a much smaller thermal conductance than the observed diffusion so the latter is not a mere artefact of losses.

B. Spin conductance

Here we discuss the uncertainty in the obtained spin conductances, particularly concerning the apparent spin transport induced by atom losses.

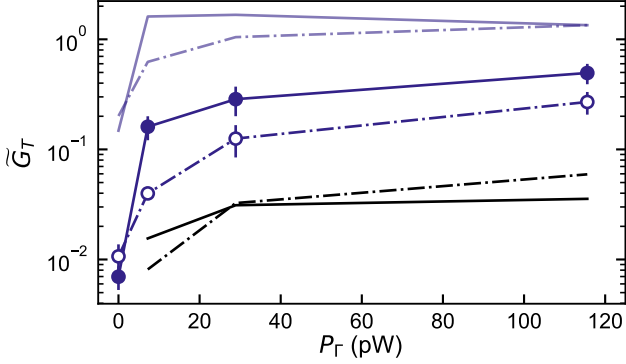


FIG. S3. **Limits of fitted thermal conductances.** Data points are the same as in Fig. 4C. Filled (open) symbols correspond to spin-dependent (pairwise) dissipation. Lines in lighter navy correspond to the estimated upper bound within the phenomenological model given by Eq. S12. Black lines correspond to the apparent thermal conductances assuming no real transport but only particle losses from the reservoirs given the measured particle loss rate.

Given that the two dissipation mechanisms lead to very similar spin conductances with respect to the loss current (Fig. 4C, inset), we explain the idea using pairwise dissipation for simplicity. We can consider two extreme scenarios: 1) If the pairwise dissipation can only remove a pair with initial correlation, i.e., both atoms are arriving from the same reservoir, then the dissipation cannot change the magnetization M_i in either reservoir. Thus the losses do not directly induce an apparent spin current. 2) If the pairwise dissipation *always* removes a pair with constituents coming out of different reservoirs (in the picture of Fig. 3A, always photoassociating a $|\uparrow\rangle$ atom from the left reservoir with a $|\downarrow\rangle$ atom from the right reservoir), dissipation alone leads to apparent spin current. Effectively, each spin exhibits a loss-induced apparent decay of $\Delta N_{\uparrow(\downarrow)}(t) = \Delta N_{\uparrow(\downarrow)}(0)e^{-\gamma_N t}$. This corresponds to $\Delta M(t) = \Delta M_0 e^{-\gamma_N t}$. In fact, γ_N is very close to $1/\tau_\sigma$, the observed decay rate of ΔM .

However, considering the channels length being considerably larger than the dissipation beam size, the first scenario appears physically much more plausible than the second scenario. Thus, we believe that the observed spin diffusion is real transport rather than purely arising from losses.